JOURNAL OF PROPULSION AND POWER
Vol. 23, No. 5, September–October 2007

Characterization and Performance Enhancement of Submerged Inlet with Flush-Mounted Planar Side Entrance

Shu Sun,* Rong-wei Guo,† and Yi-zhao Wu‡
Nanjing University of Aeronautics and Astronautics, 210016 Nanjing, People's Republic of China

DOI: 10.2514/1.26432

Previous investigations show that it is not easy for the freestream to enter a submerged inlet with flush-mounted planar side entrance. To improve the performance of this type of inlet, three important entrance parameters, side edge angle, ramp angle, and characteristic parameter of aft lip, are introduced in this paper, and their effects on the performance of the inlet are studied by both experiments and computational fluid dynamics. Based on the results, a submerged inlet with a trapezoid entrance is designed and tested over a wide range of flow conditions. Results indicate that the designed submerged inlet can give excellent performance at the design condition and provide satisfactory performance over a wide range of test conditions. By using a numerical analysis, the influences of the freestream Mach number, the angle of attack, yaw, and Mach number at the exit on the performance and flow structure of the submerged inlet have been obtained.

Nomenclature

a	=	constant radius of lemniscate function
C_p	=	static pressure coefficient
D	=	diameter of the exit
L	=	length of the submerged inlet
M_e	=	Mach number at the exit*
M_0	=	freestream Mach number
P^*_{Avg360}	=	mass-average total pressure over the entire engine face
$P^*_{\mathrm{min\,60}}$	=	minimum mass-average total pressure over any 60 deg sector around the centroid of the fan face
P^*_{rms}	=	mean square root of fluctuation total pressure around the engine face
P^*_0	=	freestream total pressure
W	=	synthetic flow distortion index
Y	=	offset of the submerged inlet
α	=	angle of attack
β	=	yaw
$\overline{\Delta\sigma_0}$	=	circumferential total pressure distortion index
ε	=	dynamic total pressure distortion index
θ	=	characteristic parameter of aft lip
ξ	=	side edge angle
σ	=	total pressure recovery coefficient
ψ	=	ramp angle

Subscripts

Avg	=	average value
e	=	exit
0	=	freestream

Superscript

*	=	total or stagnation condition

Received 10 July 2006; revision received 14 May 2007; accepted for publication 16 May 2007.

*Post-Doctor, College of Aerospace Engineering.
†Professor, College of Power and Engineering.
‡Professor, College of Aerospace Engineering.

Introduction

BECAUSE of their advantageous geometrical characteristics, submerged inlets have received considerable attention. This type of inlet is superior to conventional nacelle-mounted inlets due to decreased external drag and minimization of foreign object damage. However, because the inlets are entirely embedded in an air vehicle body, the outside boundary layer is almost entirely ingested into the inlets, which results in low total pressure recovery and high flow distortion [1,2]. Thus, in the early 1940s, research studies were initiated for the so-called NACA submerged inlets [1–5], which were employed only for the auxiliary applications in the aircraft [3–5]. Since then, great efforts have been made to improve the performance of this type of inlet mounted on the cylinder so that it can be used as the main air induction system of the propulsion engine [6–12]. As a result, some examples of this type of inlet were employed on several air vehicles. Today, with the ever-increasing demand for high survivability, a submerged inlet combined with the stealthy fuselage featuring flat surfaces is the common choice for most hi-tech air vehicles. But in this combination, it is not easy for the oncoming flow to enter the inlet due to the lack of favorable three-dimensional effects particular to the cylinder-shaped aircraft applications. In fact, in the 1980s preliminary computational and experimental studies demonstrated that a two-dimensional submerged inlet performed badly with lower total pressure recovery and less mass flow rate [13,14]. Then, at the beginning of this century, a submerged inlet with finite width for a stealthy uninhabited combat air vehicle (UCAV) was designed by Yu [15]. It was found in the experiment that the inlet could deliver sufficient mass flow to the engine. Furthermore, this study was followed by extensive numerical simulations and low speed wind-tunnel tests which revealed that the counter-rotating vortex pair [16–19] generated by the side edges of the entrance was one of the main impetuses that sucked the airflow into the submerged inlet [15]. Nevertheless, this inlet exhibited excessive total pressure loss and flow distortion [15] according to the experimental results obtained by Yu.

To improve the critical system-level performance metrics of total pressure recovery and flow distortion, it is important to obtain the parametric trends of key design variables and to establish an engineering design methodology. In this paper, three important entrance parameters are introduced and their effects on the performance of the submerged inlet integrated with a stealthy fuselage are obtained. Furthermore, a new shape is designed through selecting a suitable group of entrance parameters and its performance and flow structure are investigated by both experiments and computational fluid dynamics (CFD) over a wide range of flight conditions.

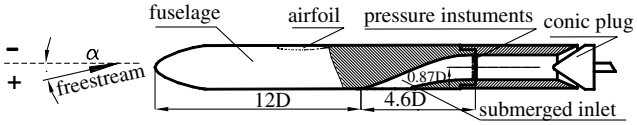

Fig. 1 Sketch of the inlet model.

Methodology

Experimental Setup

The inlet studied is placed at the aft part of the fuselage which is of a trapezoidal cross section. The distance from the apex of the fuselage to the leading edge of the inlet is $12D$, where D is the diameter of the exit section of the inlet. As shown in Fig. 1, the total length of the inlet is $4.6D$, and the vertical offset is $0.87D$, which is the distance between the center point of the exit and the belly of the fuselage.

The wind-tunnel test model with a total length of 1000 mm includes the fuselage, a submerged inlet, pressure instruments, and a conic flow plug, as illustrated in Fig. 1. Because of the constraints of wind-tunnel blockage and internal flow measurement, the wings are not taken into consideration.

The exit measurement plane of the inlet contains a 40-point total pressure rake and four static ports to measure total pressure recovery, flow distortion, and mass flow. The rake consists of eight branches, spaced at 45 deg intervals around the exit. Each branch has five pressure sampling tubes, made of 0.8 mm-diam stainless steel tubes. The probe tips, which are on rings of equal area, extend 5 mm ahead of the juncture to minimize disturbance. All pressures are measured by an electronically scanned pressure transducer system (ESP). The pressures obtained from the ESP have a margin of error of 0.05% over the full range of calibration. Four Kulite gauges are placed counter-clockwise at 22.5, 157.5, 202.5, and 337.5 deg, respectively, along the circumference to obtain high-frequency information. In addition, the mass flow plug, placed at the model exit and driven by an electric motor, provides flow control for measurements at different mass flow ratios.

The experiments were performed in the NH-1 high-speed wind tunnel at Nanjing University of Aeronautics and Astronautics (Fig. 2). The test section is a 600 mm × 600 mm square. The unit Reynolds number of the wind tunnel ranges from 1.2×10^7/m to 1.77×10^7/m. During the tests, the freestream Mach number varies from 0.50 to 0.80, the angle of attack from −2 to 8 deg and the yaw from 0 to 6 deg.

In this paper, the customary mass-average total pressure recovery coefficient σ ($P^*_{\text{Avg360}}/P^*_0$, where P^*_{Avg360} is the mass-average total pressure over the entire engine face and P^*_0 is the freestream total pressure) is used to qualify the pressure recovery performance of the inlet. In addition, to qualify the uniformity of the total pressure map at the engine face, the circumferential total pressure distortion index $\overline{\Delta\sigma}_0$ is calculated as follows:

$$\overline{\Delta\sigma}_0 = (1 - P^*_{\text{min 60 deg}}/P^*_{\text{Avg360}}) \times 100\%$$

where $P^*_{\text{min 60 deg}}$ is the minimum mass-average total pressure over any 60 deg sector around the centroid of the fan face.

Furthermore, the synthetic total pressure distortion index W, a common criterion in Russia, is also used in this paper. This index contains the above circumferential total pressure distortion index $\overline{\Delta\sigma}_0$ and the dynamic total pressure distortion index ε. The performance indices W and ε are defined as follows:

$$\varepsilon = P^*_{\text{rms}}/P^*_{\text{Avg360}} \times 100\% \qquad W = \overline{\Delta\sigma}_0 + \varepsilon$$

where P^*_{rms} is the mean square root of fluctuation total pressure around the engine face.

By such definitions, circumferential distortion levels less than 5.0% and the synthetic distortion levels lower than 8.5% are generally considered to be acceptable.

Fig. 2 Submerged inlet installed in NH-1 600 mm × 600 mm wind tunnel.

Numerical Approach

In the paper the FLuent flow analysis software is used for the flowfield predictions. The Reynolds-averaged compressible time-dependent Navier=Stokes equations in three dimensions are solved by using a finite-volume spatial discretization in which the state variables are stored at the cell center. In the computations, the inviscid flux scheme is Roe's method, and the monotonic upwind scheme for conservation laws (MUSCL) approach is used for variable extrapolation. Turbulence is modeled by the k–ε equations. A steady-state solution is obtained through the Gauss–Seidel relaxation.

To eliminate the boundary effects on the CFD results, a large column flow domain, with $20D$ in diameter and $30D$ in length, is chosen, and the channel zone is extruded $2D$ at the actual exit of the inlet. Additionally, no-slip adiabatic boundary conditions are imposed on the solid walls, and characteristic boundary conditions using Riemann invariants are applied to the far field. For the pressure outlet condition at the exit of the inlet, a backpressure is specified.

In the flow domain the truncation error highly depends on the grid resolutions. Therefore, it is important to choose a grid size that is sufficiently fine to solve the flow domain accurately for this specific problem and that is small enough to save computational time. To determine the grid sensitivity involved in the numerical study of the submerged inlets, a sequence of three grids with increasing resolution is used. For each grid size, the grid topology used for the computations contains 21 blocks which match each other exactly and compose the complex flow domain. Figure 3a shows a close-up view of the surface grids around the entrance of the inlet. A side view of the grids on the symmetry plane and the exit plane is presented in Fig. 3b. By specifying the first cell height and the stretching ratio, we ensure that there is a clustering near the wall region and the channel zone. Table 1 shows the number of cells and the corresponding performance at the engine face of a specific submerged inlet. By comparing the values of σ and $\overline{\Delta\sigma}_0$ in Table 1, it can be seen that the difference between 1,200,000 cells and 900,000 cells is 2.2% for the total pressure recovery and 4.3% for the circumferential distortion index. That is to say, the truncation errors are acceptably small for the submerged inlet. Thus, a grid of 900,000 nodes is adopted in the subsequent numerical analysis.

Results and Discussion

Trends of the Entrance Design Parameters

This paper conducts a trade study for a range of possible entrance design parameters of the submerged inlets. The influences of three entrance parameters, side edge angle ξ, ramp angle ψ, and aft lip characteristic parameter θ (Fig. 4), are obtained by varying one design parameter and keeping the two other parameters constant under the same constraints of the fuselage and freestream condition ($M_0 = 0.7$, $\alpha = 0$ deg, $\beta = 0$ deg). The purpose of the trade study is to gain physical insight into the effects of the entrance parameters on the performance of the inlet and to find suitable entrance

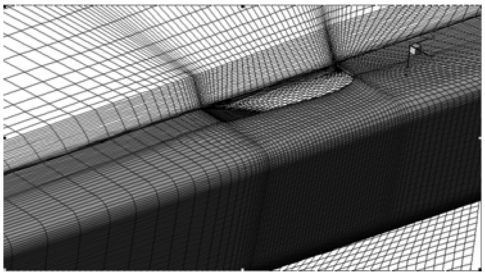

a) Surface grids around the entrance of the inlet

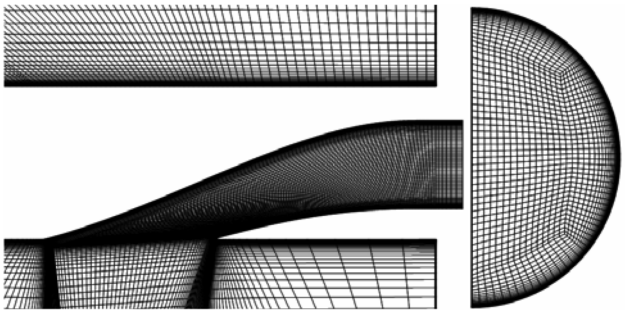

b) Grids of the symmetry plane

Fig. 3 Grids of the submerged inlets on the plane.

parameters for achieving lower total pressure loss and flow distortion at the exit.

Part 1: Influence of the Side Edge Angle ξ

From the development of secondary flow vectors along the duct [16,17], it can be seen that a counter-rotating vortex pair [16–19] originating from side edges of the entrance induces an upward velocity component which sucks the main flow into the duct. Moreover, the vortical structure has remarkable impact on the distribution of the low total pressure region at the exit. Therefore, attempts have been made to change the vortex strength by varying the side edge angle.

Figure 5 presents the variation of the total pressure recovery coefficient with the side edge angle ξ at the fixed ramp angle $\psi = 23$ deg and characteristic parameter $\theta = 40$ deg. When the side edge angle is increased to 4 deg, the total pressure recovery achieves the highest value. It may be the result of more captured main flow due to the increase of the vortex strength. When the side edge angle continues to move up to 12 deg, the total pressure recovery decreases to less than 0.91 because of the loss from the strong mixing process instigated by the large side edge angle (Fig. 6). Additionally, it also can be observed in Fig. 5 that the CFD results agree well with the experimental data and the deviation is less than 1%.

Table 1 Grid sensitivity analysis for a specific submerged inlet

ID	No. of cells	σ	$\overline{\Delta\sigma_0}$
1	600,000	0.916	4.1%
2	900,000	0.911	4.9%
3	1,200,000	0.909	4.7%

Figure 7 displays the effect of the side edge angle on the circumferential total pressure distortion index, where the CFD and experimental values match well, and both bottom out at $\xi = 4$ deg. To interpret the tendency in Fig. 7, the total pressure recovery coefficient contour plots at the exit with three different side edge angles are shown in Fig. 8. It should be noted that, when $\xi = 0$ deg, the contour plot shows a large region of low total pressure near the top surface, which indicates a high flow distortion. With the increase of the side edge angle, the low total pressure fluid migrates from the top surface toward the bottom surface and the flow distortion index is reduced to less than 4.0% due to the fact that the accentuated vortex pair pulls the boundary layer around the engine face perimeter. When the side edge angle is increased to 12 deg, as a result of the aggravating vortex structure (Fig. 9) and the strong mixing loss, the accumulation of the boundary layer fluid near the bottom surface raises the circumferential flow distortion index to over 6.0%.

Part 2: Influence of the Ramp Angle ψ

The static pressure coefficient distribution and the velocity vector around the entrance on the symmetry plane indicate that the pressure gradient perpendicular to the freestream near the fore lip forces the coming flow to enter the inlet. Hence, it implies that the value of the ramp angle has a great influence on the performance of submerged inlets.

The sensitivity of the total pressure recovery to the ramp angle is illustrated in Fig. 10, where both the experimental and the numerical analysis indicate that the inlet with ramp angle of 23 deg yields the highest total pressure recovery when the side edge angle is 4 deg and the aft lip parameter is 20 deg. To account for the effects of this parameter, the distributions of the static pressure coefficient and Mach number on the symmetry plane with three different ramp angles are compared in Fig. 11.

As displayed in Fig. 11, the local static pressure coefficient of the fore lip near the entrance varies from −0.57 (Fig. 11a) to −1.08 (Fig. 11c), which indicates that the pressure gradient perpendicular to the freestream is stronger at a higher ramp angle, and thus more main flow is sucked into the duct. On the other hand, with the increasing ramp angle, the flow acceleration near the fore lip is intensified, and a local critical shock occurs at $\psi = 25$ deg, leading to a sharp increase in boundary layer thickness. Consequently, as the ramp angle changes from 20 to 25 deg, a small increase followed by a substantial decline in total pressure recovery coefficient can be observed in Fig. 10.

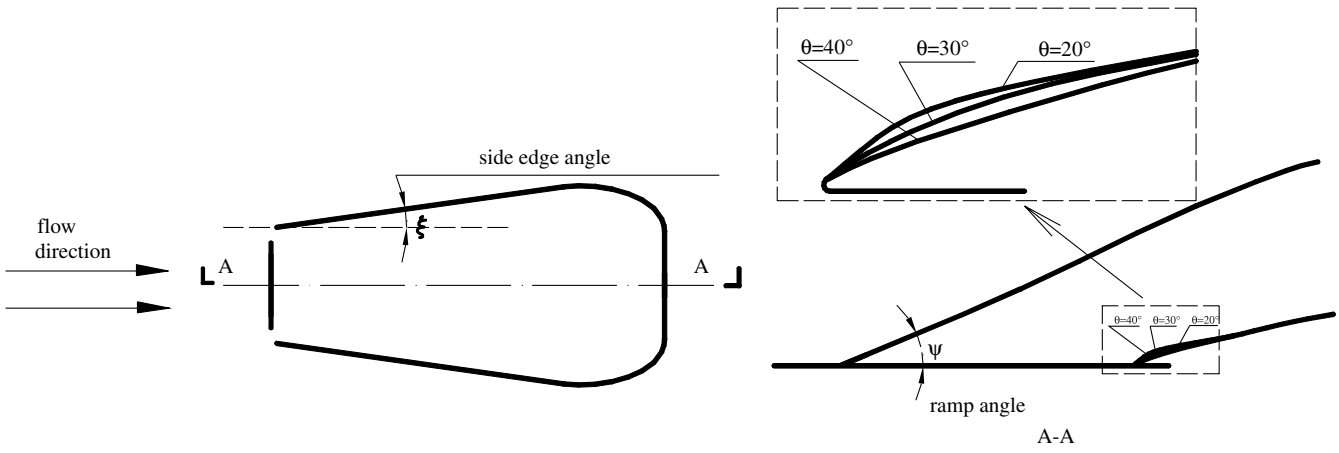

Fig. 4 Entrance parameters of the submerged inlet on the plane.

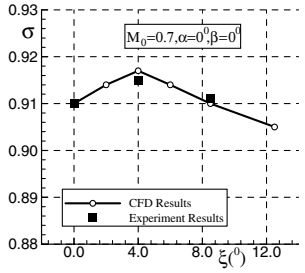

Fig. 5 Total pressure recovery coefficient versus side edge angle.

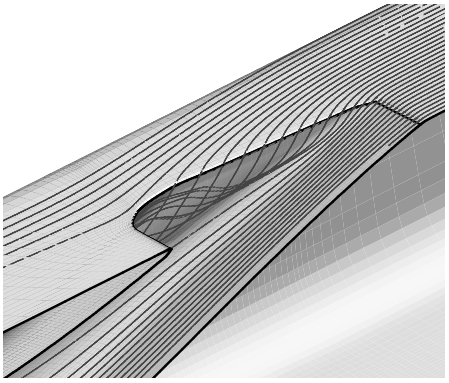

a) $\xi = 4°$

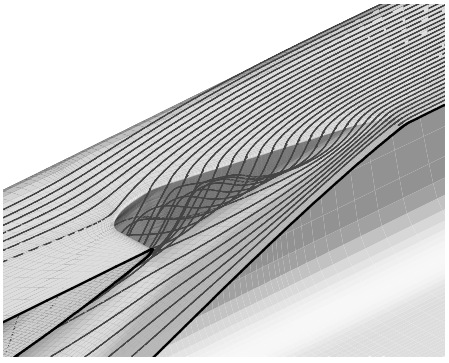

b) $\xi = 12.5°$

Fig. 6 Streamlines near the entrance with different side edge angles (CFD results).

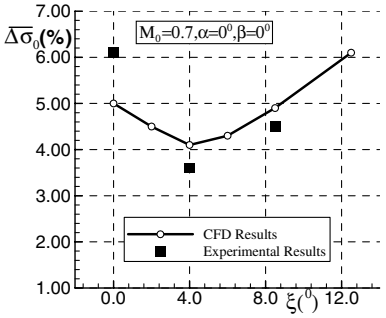

Fig. 7 Circumferential total pressure distortion index versus side edge angle.

Figure 12 presents the total pressure distortion index $\overline{\Delta\sigma_0}$ with respect to the ramp angle ψ. As shown in Fig. 12, CFD and experimental results agree well, and both achieve the lowest value at the ramp angle of 23 deg. Obviously, the ramp angle has an impact on the total pressure distributions at the exit. According to the experimental results, the high total pressure region climbs up with the increase of the ramp angle. When ψ equals 23 deg, the high total pressure region is found at the center of the exit and the boundary layer is distributed circumferentially when the other entrance parameters remain at 4 and 20 deg, respectively.

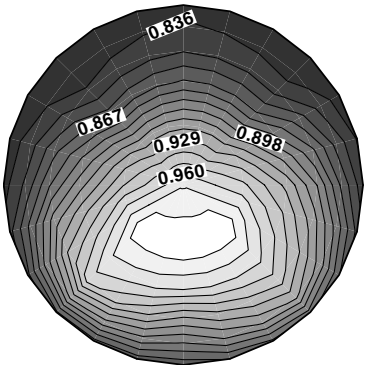

a) $\xi = 0^0$

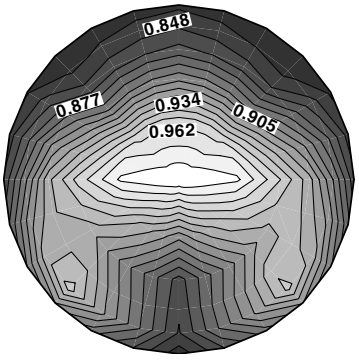

b) $\xi = 4^0$

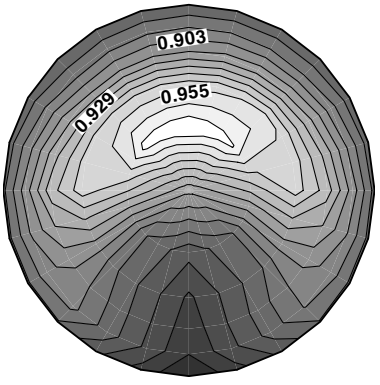

c) $\xi = 8.5^0$

Fig. 8 Contour plots of total pressure recovery at the exit with different side edge angles (experimental results).

Part 3: Influence of Aft Lip Characteristic Parameter θ

For the submerged inlet, the shape of the aft lip plays an important role in obtaining an acceptable flow distortion. In this paper, a type of lemniscate function is employed to obtain a suitable aft lip profile with the control parameters of θ and α (Fig. 13).

Similar to the ramp angle sensitivity analysis described in the preceding subsection, θ, which determines the thickness of the aft lip, is used to examine its effect on the performance of the submerged inlet on the plane. The aft lip characteristic parameter θ ranges between 20 and 40 deg. The side edge angle and ramp angle are left unchanged at 8.5 and 23 deg, respectively. The total pressure recovery coefficient and circumferential distortion index are showed in Table 2. Although the total pressure recovery is not sensitive to the change in θ, the circumferential distortion index is highly affected

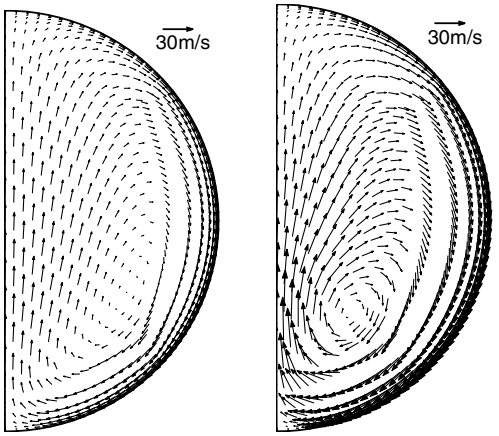

Fig. 9 Secondary flow at the exit with different side edge angles (CFD results).

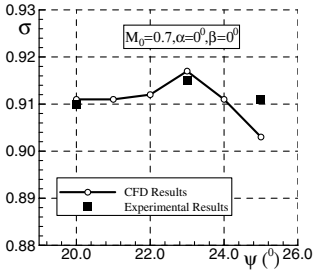

Fig. 10 Total pressure recovery coefficient versus ramp angle.

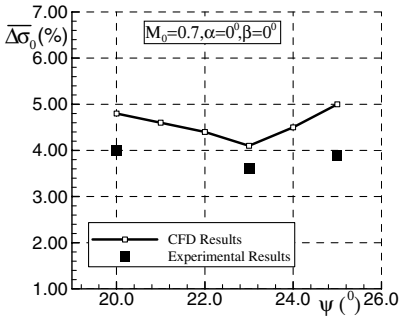

Fig. 12 Circumferential total pressure distortion index versus ramp angle.

and the minimum distortion is obtained at $\theta = 30$ deg. As θ decreases from 40 to 30 deg, the local pressure gradient perpendicular to the freestream increases due to the increase of the area contraction near the aft lip, which deflects the local core flow downward and pulls the boundary layer evenly around the engine face.

In summary, the flow distortion of submerged inlets is sensitive to the side edge angle, the ramp angle, and the shape of the aft lip. The total pressure recovery is also apparently affected by the first two parameters. Therefore, the cooperation of these three entrance parameters is important for the performance enhancement of the submerged inlet.

Characteristics of a Newly Designed Submerged Inlet on the Plane

A submerged inlet on the plane with the side edge angle of 4 deg, the ramp angle of 23 deg, and the characteristic parameter of the aft lip of 30 deg is designed and tested in a high-speed wind tunnel to obtain performance enhancement and characterization. Table 3 gives the detailed geometry information of the inlet studied.

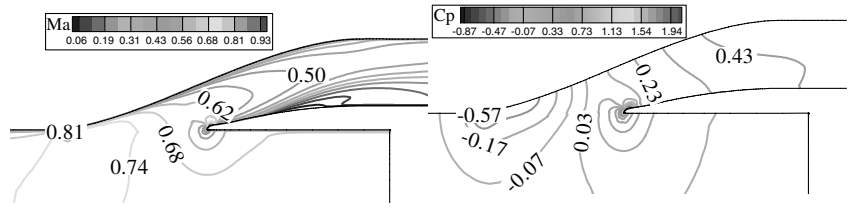

a) $\psi = 20^0$

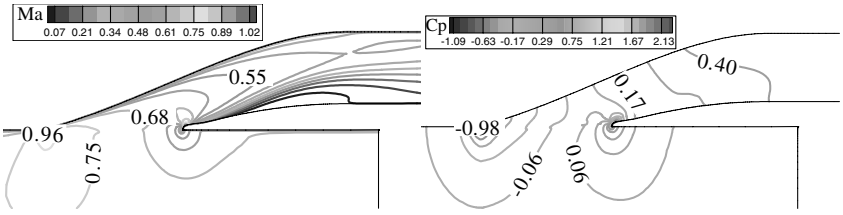

b) $\psi = 23^0$

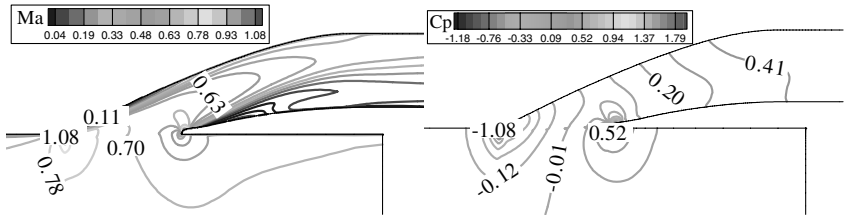

c) $\psi = 25^0$

Fig. 11 Distributions of static pressure coefficient and Mach number on the symmetry plane with different ramp angles (CFD results).

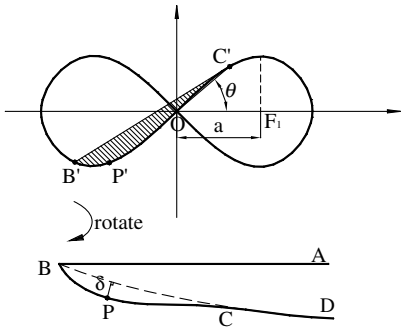

Fig. 13 Sketch of the aft lip (upside down).

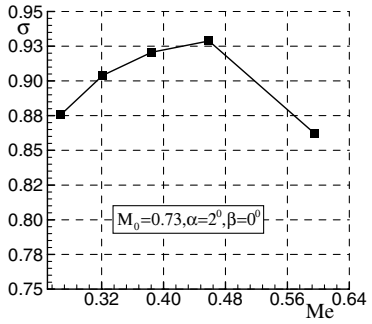

Fig. 14 Total pressure recovery coefficient versus Mach number at the exit (experimental results).

Through the experiments and the computations, the performance and the flow structure of the improved inlet under different exit Mach numbers, angles of attack, yaws, and freestream Mach numbers are obtained.

Effects of the Mach Number at the Exit

Unlike pitot inlets or S-shaped inlets [19], the capture area of the submerged inlet is difficult to determine. Thus, the Mach number at the exit is used instead of the mass flow ratio in the analysis. Figure 14 presents the relation between the total pressure recovery coefficient and the Mach number at the exit. Because less low-energy flow near the fuselage enters the inlet compared to the total mass flow captured at a higher M_e (Fig. 15), the total pressure recovery coefficient increases gradually and reaches 0.923 when $M_e = 0.4$. When the Mach number at the exit is larger than 0.48, a sharp drop in the total pressure recovery occurs. This is due to the increased friction loss, mixing loss, and possible separation loss.

Figure 16 shows the variations of the circumferential and the synthetic total pressure distortion indices with the Mach number at the exit. In spite of an obvious upward shift of $\overline{\Delta\sigma_0}$ and W at higher exit Mach numbers, both indices are only 2.1% and 4.9% at the design condition ($M_0 = 0.73$, $\alpha = 2$ deg, $\beta = 0$ deg, $M_e = 0.4$) and do not exceed the acceptable distortion level until $M_e = 0.5$. Figure 17 gives the total pressure distributions at the engine face of two different Mach numbers at the exit. It can be inferred that, at the design condition, the submerged inlet with carefully selected entrance parameters can produce a vortical flow structure and a pressure gradient that make the boundary layer around the engine face. However, at a higher M_e such as 0.59, a large region of low total pressure appears due to the flow deterioration near the aft lip induced by the sharp turn of the local stream tube and the strong vortex interactions.

Table 2 Impact of the lip thickness on the inlet performance (experimental results) ($\xi = 8.5$ deg, $\psi = 23$ deg)

ID	θ	σ	$\overline{\Delta\sigma_0}$
1	40 deg	0.911	4.5%
2	30 deg	0.912	3.1%
3	20 deg	0.911	3.8%

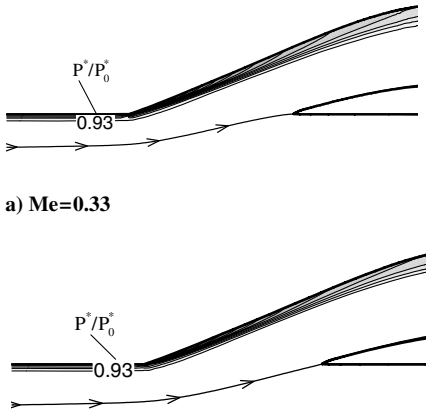

Fig. 15 Captured flow tube of different Mach numbers at the exit (CFD results).

Effects of the Freestream Mach Number

Figure 18 illustrates the effects of the freestream Mach number on the total pressure recovery coefficient. It shows that the recovery coefficient decreases with the increase of the freestream Mach number because the coming boundary layer of the inlet is thickened due to the increase of the adverse pressure gradient downstream of the nose of the fuselage (Fig. 19). For a freestream Mach number larger than 0.73, the recovery coefficient decreases more rapidly. This trend probably arises from a local shock (Fig. 20) occurring near the fore lip of the inlet, which accelerates the development of the local boundary layer and deteriorates the internal flow.

According to the test results, the total pressure distribution at the exit is not sensitive to the change of the freestream Mach number except for slight differences on the minimum total pressure value. As shown in Fig. 21, when the freestream Mach number is below 0.8, the circumferential and the synthetic distortion indices vary slightly and are found to fall in the acceptable range of 5.0 and 8.5%, respectively. Unfortunately, when the freestream Mach number reaches 0.9, the low momentum fluid, aggravated by the shock/boundary layer

Table 3 Geometry parameters of the newly designed inlet

Parameters	Values
Diameter at the exit	D
Total length of the inlet	4.6D
Offset of the inlet	0.87D
Area shape distribution	Polynomial spline with modest turning
Centerline distribution	Special polynomial spline
Entrance of the inlet	Trapezoid
Ramp angle	23 deg
Side edge angle	4 deg
Characteristic parameters of aft lip	40 mm, 30 deg

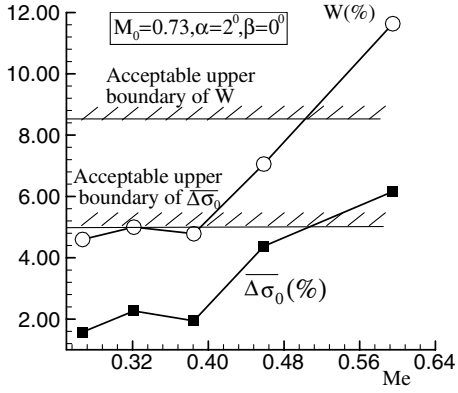

Fig. 16 Circumferential and synthetic total pressure distortion indices versus the Mach number at the exit (experimental results).

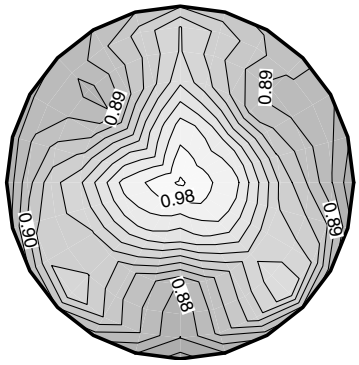

a) $M_e = 0.4$

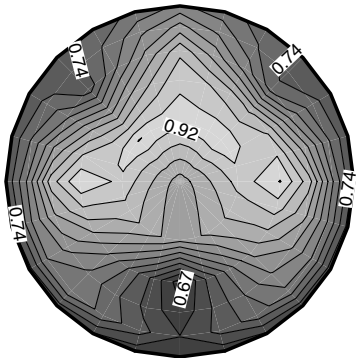

b) $M_e = 0.59$

Fig. 17 Contour plots of total pressure recovery coefficient at the engine face (experimental results).

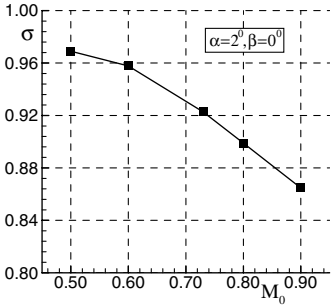

Fig. 18 Total pressure recovery coefficient versus freestream Mach number (experimental results).

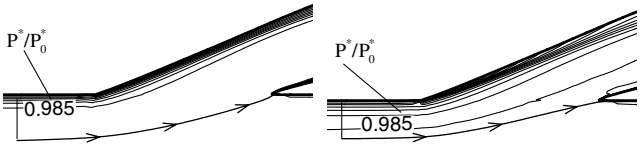

a) $M_0 = 0.5$ **b) $M_0 = 0.8$**

Fig. 19 Captured flow tube at different freestream Mach numbers (CFD results).

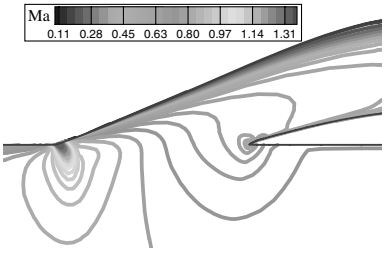

Fig. 20 Mach number distributions on the symmetry plane at $M_0 = 0.8$ (CFD results).

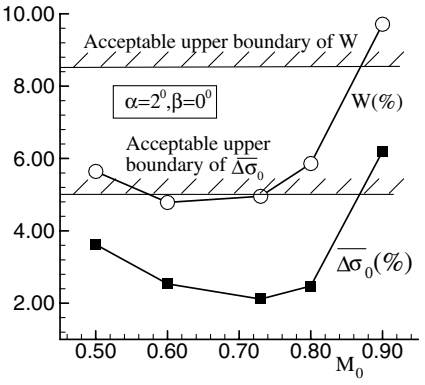

Fig. 21 Circular and synthetic total pressure distortion indices versus freestream Mach number (experimental results).

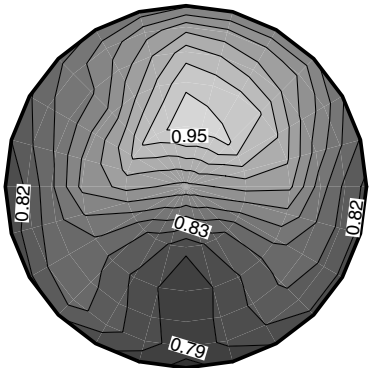

Fig. 22 Contour plot of total pressure recovery coefficient at the engine face at $M_0 = 0.90$ (experimental results).

interation near the fore lip, accumulates on the bottom surface and is contained in the maximum distortion 60 deg sector (Fig. 22). As a result, both distortion indices reach a high level, which may threaten the stable operation of the engine.

Effects of the Angle of Attack

Figure 23 demonstrates the variation of the total pressure recovery coefficient with the angle of attack (ranging from −2 to 8 deg). It can be observed that, with the increase of the incidence, the total pressure

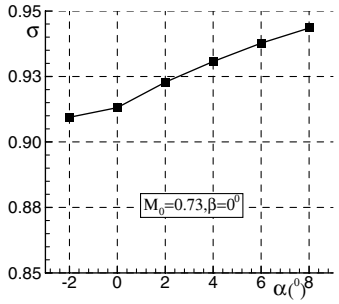

Fig. 23 Total pressure recovery coefficient versus angle of attack (experimental results).

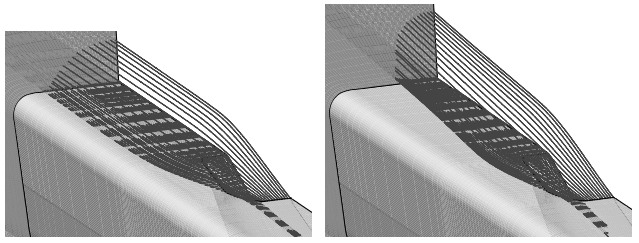

$\alpha = 0^0$ $\alpha = 8^0$

Fig. 24 Stream tubes captured by the submerged inlet at different incidences (CFD results).

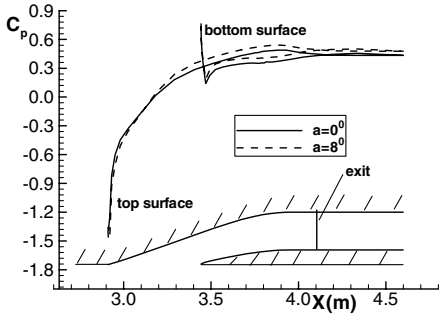

Fig. 25 Static pressure coefficient along the wall (CFD results).

recovery goes up and approaches 0.95. This tendency is interpreted as follows: with the increase of the angle of attack, the entrance of the submerged inlet exposes to the freestream gradually and captures more of the freestream. Furthermore, for a higher incidence the upwash flow around the fuselage sweeps part of the oncoming boundary flow away from the inlet, which also leads to the increase of σ. Figure 24 gives a clear picture of the effects of a positive angle of attack. Obviously, the cross section of the captured stream tube appears much taller and narrower at $\alpha = 8$ deg than at $\alpha = 0$ deg, which suggests that more high-energy flow and less low-energy flow are sucked into the duct at a higher angle of attack.

The static pressure coefficient distributions along the top and bottom surfaces when $\alpha = 0$ deg and $\alpha = 8$ deg are shown in a nondimensional form in Fig. 25, where few differences can be seen in the streamwise pressure gradient within the duct. This implies that the angle of attack has the main impact on the stream tube captured by the submerged inlet but slight influence on the internal flow structure. Hence, the performance improvement of the submerged inlet is expected to strongly depend on the management of the boundary layer along the fuselage.

As shown in Fig. 26, with the increase of the angle of attack from -4 to 8 deg, the circumferential distortion index and the synthetic distortion index remain below 2.8 and 5.6%, respectively, both of which are far less than the typical engine tolerance. This indicates that an acceptable performance over a wide range of flow conditions

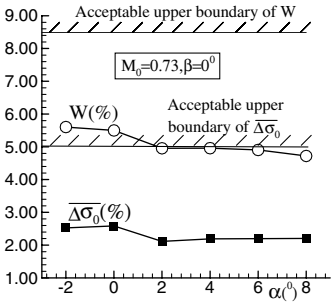

Fig. 26 Circumferential and synthetic total pressure distortion indices versus angle of attack (experimental results).

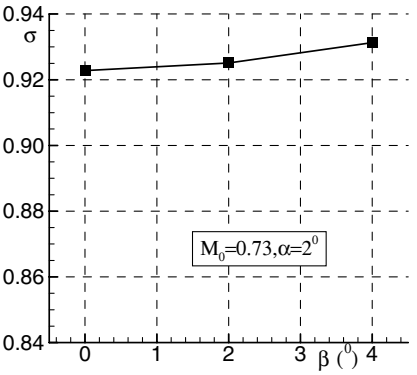

Fig. 27 Total pressure recovery coefficient versus yaw (experimental results).

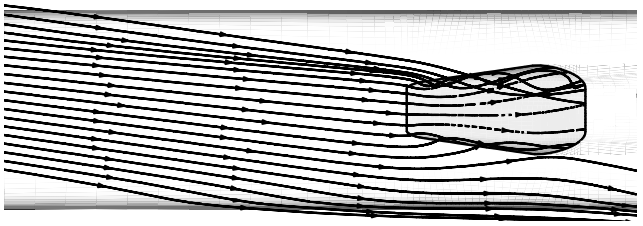

Fig. 28 Streamlines near the fuselage while $\beta = 4$ deg (CFD results).

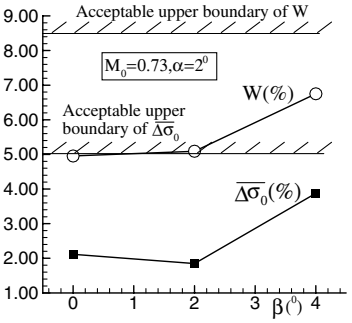

Fig. 29 Circumferential and synthetic distortion indices versus yaw (experimental results).

can be achieved for the submerged inlet with flush-mounted planar side entrance by carefully selecting the entrance parameters.

Effects of the Yaw

Effects of the yaw on the total pressure recovery coefficient are displayed in Fig. 27. With the increase of the yaw up to 4 deg, the

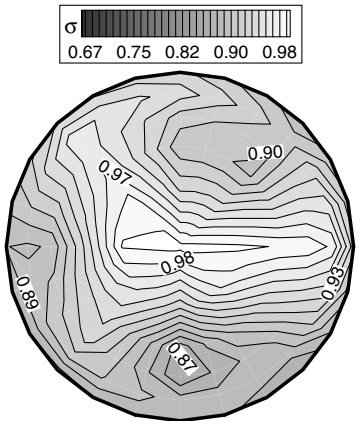

Fig. 30 Contour plot of total pressure recovery coefficient at the engine face (experimental results).

total pressure recovery increases gradually due to the reduction of the developing length of the boundary layer along the fuselage (Fig. 28).

According to Fig. 29, the circumferential and the synthetic distortion indices are acceptable though both increase with the rise of the yaw.

In Fig. 30, the total pressure contour plot of the engine face at the yaw of 4 deg is presented. Compared with Fig. 17, the low total pressure fluid at the exit in this figure shifts in a counter-clockwise direction due to the dominating vortex structure from the lee side.

Summary

This paper presents an experimental and computational study on the key design parameters of submerged inlets with flush-mounted planar side entrance. Based on these results, a submerged inlet with trapezoid entrance is designed and investigated over a wide range of flight conditions by both experiments and numerical simulations. The conclusions drawn from this study can be summarized as follows:

1) Entrance parameters, ψ, ξ, and θ, are found to have significant impacts on the aerodynamic performance of the submerged inlet. Both the total pressure recovery and the flow distortion indices achieve the optimal value at $\xi = 4$ deg, $\psi = 23$ deg, and $\theta = 40$ deg. As to the ramp angle, any deviation from 23 deg yields an unfavorable influence on the performance of the inlet. The circumferential distortion index is highly affected by the characteristic parameter θ of the aft lip and bottoms out at $\theta = 30$ deg, though the total pressure recovery almost remains constant over the tested range.

2) For the freestream Mach number ranging from 0.5 to 0.8, the circumferential and the synthetic distortion indices are both well below 80% of the maximum acceptable value in spite of the apparent decline of the total pressure recovery coefficient. However, for the freestream Mach number of 0.9, both of the distortion indices ascend rapidly to a high level, which may threaten the stable operation of the engine.

3) For the inlet embedded into the belly of the fuselage, the increase of the angle of attack is beneficial to both the total pressure recovery and the distortion indices over the tested range. Furthermore, the total pressure recovery coefficient rises gradually with the increase of the yaw and the distortion indices are still within a tolerable level despite the unfavorable effects of the yaw.

4) The experimental results confirm the excellent performance of the newly developed submerged inlet based on the knowledge of effects of the entrance parameter. When $M_0 = 0.5$–0.8, $\alpha = -2$–8 deg, and $\beta = 0$–4 deg, the total pressure recovery varies from 0.886 to 0.980, the circumferential total pressure index varies from 1.4 to 4.4%, and the synthetic distortion index varies from 3.5 to 7.7%.

Acknowledgments

This work is supported by the National Science Foundation for Post-doctoral of the People's Republic of China through Grant No. 0601042B and the Jiangsu Post-doctoral Sustentation Fund, People's Republic of China, through Grant No. 20060400935.

References

[1] Seddon, J., and Goldsmith, E. L., *Intake Aerodynamics*, 1st ed., AIAA Education Series, Collins Professional and Technical Books, AIAA, New York, 1985, Chaps. 1, 11.

[2] Goldsmith, E. L., and Seddon, J., *Practical Intake Aerodynamics Design*, 1st ed., AIAA Education Series, Collins Professional and Technical Books, AIAA, New York, 1993, Chaps. 1, 2.

[3] Randall, L. M., and Mossman, E. A., "An Experimental Investigation of the Design Variables for NACA," NACA RM-A7130, Jan. 1948.

[4] Frick, C. W., Davis, W. F., Randall, L. M., and Mossman, E. A., "An Experimental Investigation of NACA Submerged-Duct Entrances," NACA ACR-5120, Nov. 1945.

[5] Sacks, A. H., and Spreiter, J. R., "Theoretical Investigation of Submerged Inlets at Low Speed," NACA TN-2323, Aug. 1951.

[6] Taskinoglu, E., and Knight, D., "Numerical Analysis of Submerged Inlets," AIAA Paper 2002-3147, June 2002.

[7] Taskinoglu, E., and Knight, D., "Design Optimization for Submerged Inlets, Part 1," AIAA Paper 2003-1247, Jan. 2003.

[8] Taskinoglu, E., Jovanovic, V., Elliot, G., and Knight, D. D., "Design Optimization for Submerged Inlets, Part 2," AIAA Paper 2003-3926, June 2003.

[9] Taskinoglu, E., "A Multiobjective Shape Optimization for a Subsonic Submerged Inlet," Ph.D. Dissertation, Rutgers University, Piscataway, NJ, May 2004.

[10] Jovanovic, V. J., Taskinoglu, E., Knight, D., and Elliott, G., "Experimental Investigation of a Submerged Inlet," AIAA Paper 2004-2649, May 2004.

[11] Taskinoglu, E. S., and Knight, D., "Multi-Objective Shape Optimization Study for a Subsonic Submerged Inlet," *Journal of Propulsion and Power*, Vol. 20, No. 4, 2004, pp. 620–633.

[12] Lee, J. G., Jung, S. Y., and Ahn, C. S., "Numerical Simulation of Three-Dimensional Flows for Flush Inlet," AIAA Paper 2004-5190, Aug. 2004.

[13] Yang, A. L., and Guo, R. W., "Numerical Simulation of the Flow of Two-Dimensional Submerged Air Inlet," *Acta Aeronautica et Astronautica Sinica*, Vol. 20, No. 5, 1999, pp. 450–454.

[14] Yang, A. L., and Guo, R. W., "An Investigation on Design and Performance for a Submerged Air Inlet," *Acta Aerodynamics Sinica*, Vol. 16, No. 2, 1998, pp. 154–161.

[15] Yu, A. Y., "A Study of the Design and Flow Characteristics for a Submerged Inlet Under a Stealthy Shaped Fuselage," Ph.D. Dissertation, Nanjing University of Aeronautics and Astronautics, Nanjing/Jiangsu, PRC, Feb. 2003.

[16] Guo, W. R., and Seddon, J., "The Swirl in an S-Duct of Typical Air Intake Proportions," *Aeronautical Quarterly*, Vol. 34, May 1983, pp. 99–129.

[17] Seddon, J., "Understanding and Countering the Swirl in S-Ducts Tests on the Sensitivity of Swirl to Fences," *Aeronautical Journal*, Vol. 88, No. 874, April 1984, pp. 117–127.

[18] Tan, H. J., and Guo, R. W., "Numerical Simulation of a Dual-Swept/Dual-Ramp Inlet Under Ground Running," *Acta Aeronautica et Astronautica Sinica*, Vol. 23, No. 3, June 2002, pp. 540–545.

[19] Tan, H. J., and Guo, R. W., "Design and Wind Tunnel Study of a Top-Mounted Diverterless Inlet," *Chinese Journal of aeronautics*, Vol. 17, No. 2, 2004, pp. 72–78.

F. Liu
Associate Editor